J Mater Sci (2023) 58:2801–2813

Materials for life sciences

Rose bengal-decorated rice husk-derived silica nanoparticles enhanced singlet oxygen generation for antimicrobial photodynamic inactivation

Nanase Mori[1], Hideya Kawasaki[1,*], Erika Nishida[2], Yukimi Kanemoto[2], Hirofumi Miyaji[2], Junko Umeda[3], and Katsuyoshi Kondoh[3]

[1] *Department of Chemistry and Materials Engineering, Faculty of Chemistry, Materials and Bioengineering, Kansai University, Suita-shi, Osaka 564-8689, Japan*

[2] *Department of Periodontology and Endodontology, Faculty of Dental Medicine, Hokkaido University, Sapporo, Hokkaido 060-8586, Japan*

[3] *Joining and Welding Research Institute, Osaka University, Ibaraki 567-0047, Japan*

Received: 30 September 2022
Accepted: 10 January 2023
Published online: 25 January 2023

ABSTRACT

Rice husks are well known for their high silica content, and the RH-derived silica nanoparticles (RH NPs) are amorphous and biocompatible; therefore, they are suitable raw materials for biomedical applications. In this study, rose bengal-impregnated rice husk nanoparticles (RB-RH NPs) were prepared for their potential photosensitization and $^1O_2$ generation as antimicrobial photodynamic inactivation. RB is a halogen-xanthene type's photosensitizer showing high singlet oxygen efficiency, and the superior photophysical properties are desirable for RB in the antimicrobial photodynamic inactivation of bacteria. To enhance the binding of anionic RB to RH NPs, we conducted cationization for the RH NPs using polyethyleneimine (PEI). The control of the RB adsorption state on cationic PEI-modified RH NPs was essential for RB RH-NP photosensitizers to obtain efficient $^1O_2$ generation. Minimizing RB aggregation allowed highly efficient $^1O_2$ production from RB-RH NPs at the molar ratio of RB with the PEI, $X_{RB/PEI.} = 0.1$. The RB-RH NPs have significant antimicrobial activity against *Streptococcus mutans* compared to free RB after white light irradiation. The RB-RH NP-based antimicrobial photodynamic inactivation can be employed effectively in treating *Streptococcus mutans* for dental applications.

Handling Editor: Andrea de Camargo.

Address correspondence to E-mail: hkawa@kansai-u.ac.jp

https://doi.org/10.1007/s10853-023-08194-z

GRAPHICAL ABSTRACT

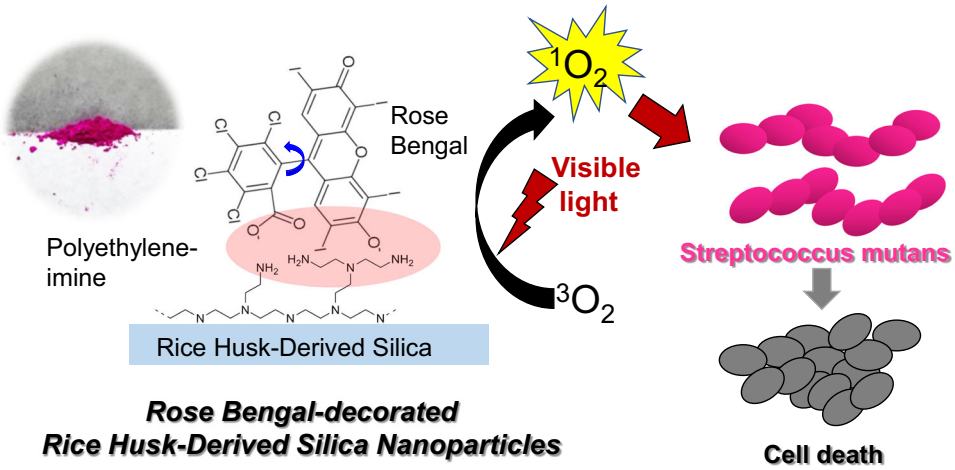

Introduction

Diseases caused by bacteria and viruses are called "infectious diseases". Among these infectious diseases, antimicrobial agents are effective against diseases caused by bacteria because they kill or inhibit the growth of the causative bacteria and other organisms, and they treat various infectious diseases [1, 2]. However, the number of "drug-resistant" bacteria that do not respond to conventional antimicrobial agents has been increasing worldwide, and various bacteria resistant to antimicrobial agents have already been identified [3]. Antimicrobial resistance (AMR) has made it increasingly difficult to prevent and treat infections [4]. As the number of resistant bacteria increases, antimicrobial drugs become ineffective, making it more difficult to treat infections that could previously be treated with appropriate therapy and recover from minor illnesses, increasing the likelihood of serious illness and even death. With the COVID-19 coronavirus pandemic, humanity has drawn concern about new antimicrobial treatments for infectious diseases.

As an alternative treatment for infectious diseases, antimicrobial photodynamic therapy (aPDT) provides no selective inactivation of pathogenic microorganisms in response to the present AMR issue [5, 6]. The inactivation mechanism of aPDT is based on a photoactivatable photosensitizer (PS) to generate cytotoxic reactive oxygen species under light irradiation of appropriate wavelengths, such as singlet oxygen ($^1O_2$) and other reactive oxygen species (ROS). Besides the ability of the non-selective inactivation, the microorganism resistance of aPDT is rarely reported, indicating the possibility of escaping AMR issues [7]. Many efforts have been focused on developing more effective organic PSs for aPDT treatment. Still, PSs have several disadvantages, such as water-solubility, photostability, biocompatibility, enzymatic degradation, and chemical modulation for specific functions.

The composite of PS with nanoparticles (NPs) can improve water-solubility, overcome aggregation issues, and protect PSs from enzymatic degradation [8–11]. Among the variety of NPs, silica-based nanomaterials have been attracted as PS support for PDT applications [12]. Silica NPs (SiOx NPS) are chemically inert and have high water dispersibility and surface modification capability. Various type's silica supports have been proposed for PDT applications, such as mesoporous SiOx NPs with the pore-integrated PSs [13–15], aggregated SiOx NPs with the pore-integrated PSs [16, 17], and covalently or physically bound complexes of PSs and SiOx NPs.[18–23]. Most of these SiOx -based nanomaterials are synthetic amorphous silica via thermal (pyrogenic) or wet routes (colloidal, precipitated, and gel) since their

particle size, shape, and porosity can be controlled during their synthetic methods. However, precursor solutions such as tetramethylorthosilicate (TMOS) and tetraethylorthosilicate (TEOS) for producing SiOx NPs are not economically and environment-friendly because of their high cost and toxicity.

Rice husks (RHs) are well known for their high silica content, and they contain organic compounds (70–80%) (including cellulose or lignin) and about 20–30% silica [24, 25]. Many rice husks are generated yearly as a byproduct of rice cultivation in a cost-effective and eco-friendly process. In recent years, the shift from fossil resources to biomass has attracted attention with the growing awareness of environmental issues such as global warming. Thus, the natural resources-based RHs have gained considerable interest in energy/ecological fields since various chemical products can be derived from RH biomass, including active carbon, silica, syngas, and biofuel [26–28]. RH-derived SiOx NPs are amorphous and biocompatible; therefore, they are suitable raw materials for biomedical applications [29–31]. However, to our knowledge, there is no study on the encapsulation of photosensitizers into RH-derived SiOx NPs for aPDT.

The present work aimed to develop the composite of Rose Bengal (RB) with RH-derived SiOx NPs (RB-RH NPs) for aPDT applications. RB is a halogen-xanthene type's PS showing intense absorption bands in the visible region of 480–550 nm, a high triplet quantum yield of 0.76, a long-lived triplet state ($t_{1/2}$ = 0.1–0.3 ms), and a high singlet oxygen quantum yield of 0.75 under 540 nm light irradiation [32]. These superior photophysical properties are desirable for RB in aPDT [13, 15, 18, 20, 22, 33]. Several studies have suggested the effectiveness of RB-based aPDT on several planktonic and biofilm-forming oral bacteria [34, 35]. RB-RH NPs confined inside the oral cavity or periodontal pockets can be excited under green light-emitting diodes (LEDs) for efficient $^1O_2$ production. These features allow the convenient and efficient a-PDT application of RB-modified RH NPs (RB-RH NPs) for oral diseases. We prepared amino-functionalized RH-derived SiOx NPs to conjugate RB through the electrostatic interaction to yield RB-RH NPs for aPDT, and the $^1O_2$ generation efficiency of RB-RH NPs depending on the RB loading amount was investigated. Finally, we demonstrate that the RB-RH NPs can reduce the bacterial proliferation of *Streptococcus mutans* after white light-emitting diode irradiation, commonly found in the human oral cavity.

Materials and methods

Materials

N,N-dimethylformamide (DMF) (assay[$HCON(CH_3)_2$](GC)min.99.5%(mass/mass)) and Rose Bengal (RB) were purchased from FUJIFILM Wako Pure Chemicals Co. 9,10-Antracenediyl-bis(-methylene) dimalonic acid (No. 75068, ABDA, ≥ 90.0%), Polyethylenimine, branched (No. 408719, average Mw ~ 800 by LS, average Mn ~ 600 by GPC) were purchased from Sigma-Aldrich Chemical Co. Methanol (99.8%) was purchased from Tokyo Kasei Kogyo Co. Pure water was purified by a water distillation apparatus (aquarius RFD250, ADVANTEC). The ultrasonic cleaner was SANSYO's D-SONiC.

Instrumentation and characterization

UV–visible (UV–Vis) absorption spectra and Fourier transform infrared (FT-IR) spectra were measured using the V-670 spectrometer (JASCO, Japan) and the FTIR 4200 spectrometer (JASCO, Japan) with an attenuated total reflection (ATR) instrument (ATR PRO ONE, JASCO, Japan)., respectively. The zeta potential was evaluated using the Zetasizer Nano ZS (Malvern Instruments Ltd., GB). Before the zeta potential measurements, all samples were dispersed by ultrasonication for 10 min. Scanning electron microscopy (SEM) and transmission electron microscopy (TEM) images were captured using a field-emission SEM apparatus (JSM-6700, JEOL, Japan) operated at an acceleration voltage of 5.0 kV and using a JEOL 1400 microscope at 120 kV. Thermogravimetric analysis (TGA) was performed using a TGA system (Thermo Plus EVO, Rigaku, Japan) at a heating rate of 5 °C/min under an airflow. To determine surface area, pore size, and pore volume, N_2 adsorption and desorption isotherm measurements were conducted using a Microtrac BELSORP-Mini instrument at 77 K under continuous adsorption conditions. Brunauer–Emmett–Teller (BET) and Barrett–Joyner–Halenda (BJH) analyses were used. The crystal nature of RH NP powders was analyzed

by X-ray diffraction (XRD, D2 PhaseRBruker AXS GmbH, Karlsruhe, Germany).

Preparation of amorphous silica NPS from rice husks (RH-NPs)

Rice husks harvested in Shiga, Japan were used as input raw materials to produce high-purity amorphous silica materials, according to the literature, where the citric acid solution leaching treatment and air combustion of rice husks are performed to remove the metallic impurities without the use of strong acids such as sulfuric acid [36, 37]. About 30 g of husks were immersed in 5 wt% citric acid solution of 500 mL at 50 °C for 30 min. The water rinsing treatment on acid-leached husks was carried out to remove the acid solution from rice husks and followed by water washing three times. The washed rice husks were dried at 100 °C for 1 h in the drying oven under an air atmosphere and then combusted at 800 °C for 30 min in the muffle furnace. The airflow rate in the combustion was 0.42 ml/s using a small air compressor.

Synthesis of PEI-modified RH NPs

To enhance the binding of RB to RH NPs, we performed cationization of RH NPs using polyethyleneimine (PEI). 0.4 g of RH NPs dispersed in 1 mL methanol was added into 5 mL methanol solution with 7.7 g PEI, and the mixture was stirred at 650 rpm all night. The solid products were isolated by centrifugation. After removing the supernatant, we added 10 mL methanol for washing and then, did the centrifugation again and repeated this procedure three times. Finally, we obtained PEI-modified RH NPs by drying the washed product under reduced pressure for 24 h.

Preparation of rose bengal-modified RH NPs (RB-RH NPs)

The RB-RH NPs are schematically summarized in Fig. 1. RB-RH NPs were prepared as follows: 20 mg of PEI-modified RH NPs was added to aqueous RB solutions (2 mL) of various concentrations (3.5×10^{-2} mg/mL, 7.0×10^{-2} mg/mL, 1.75×10^{-1} mg/mL, and 7.0×10^{-1} mg/mL) [i.e., molar ratio of RB/PEI polymer, $X_{RB/PEI} = 0$, 0.1, 0.25, and 1.0, respectively], and the mixture was stirred at 500 rpm for 1 h. Here, we regard the molecular weight of PEI as ~ 800. The anionic RB binds to the cationic PEI-modified RH NPs, producing RB-RH NPs. The RB-RH NPs were obtained as a precipitate after centrifugation at 600 rpm for 5 min, followed by washing with 25 mL water, and further centrifugation multiple times until the absorbance of washing solution was measured to be less than 0.01. Finally, dried powdered RB-RH NPs were obtained by vacuum drying.

Detection of $^1O_2$

ABDA was used as a probe to detect $^1O_2$ under excitation by a white light-emitting diode (LED) (SPF-D2, Shodensha, Japan). ABDA can react irreversibly with $^1O_2$, which causes a decrease in the ABDA absorption at 379 nm. An aqueous suspension of RB-RH NPs (1.8 mL, ~ RB absorbance of 0.1 at 665 nm) was mixed with ABDA in DMF (0.5 mM, 0.2 mL), and the final concentration of ABDA was adjusted to be 50 μM according to the references [16]. The RB absorbance of around 0.05 at 570 nm was selected to obtain dispersed RB-RH NP solution. The ABDA absorbance of the solution at 379 nm was monitored at 5 min intervals by UV–Vis spectra during the LED irradiation at a room temperature of 24 °C. We collected the same sample every 5 min to acquire UV–Vis absorption spectra. A photograph of the lighting apparatus is shown in Figure S1. The temperature increase was small to be 1.5 °C during the LED illumination for 20 min. The possible absorption from the RB-RH NP scattering backgrounds was subtracted from the UV–Vis spectra of RH NPs.

Antimicrobial effects of RB-RH NPs under white LED irradiation

RB-RH NPs were dispersed in a suspension of *Streptococcus mutans* (ATCC 35,668). The concentration of *Streptococcus mutans* is 1×10^7 CFU (colony-forming units)/mL (culture medium). The *Streptococcus mutans* suspension was dispensed into 48-well microplates at 200 μL/well. In the experimental group, RB-RH NPs and RB are added directly to the *Streptococcus mutans* suspension. Before incubation, the suspension was irradiated with white LED for 1 min. After incubation at 37 °C under anaerobic conditions for 24 h, the bacterial turbidity was determined using a turbidimeter (CO7500

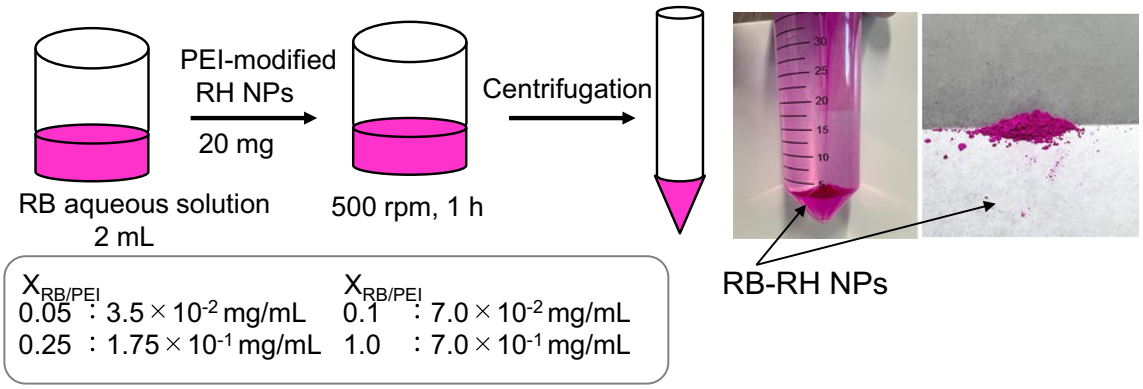

Figure 1 Preparation procedures of rose bengal modified RH NPs (RB-RH NPs).

Colorwave, Funakoshi Co., Ltd., Tokyo, Japan) at 590 nm. Scheffe's test performed the statistical analysis, and P values < 0.05 were considered statistically significant. All statistical analyses were performed using a software package (SPSS 11.0, IBM Corporation, Armonk, NY). For comparison, we also examined antibacterial tests on RB only. We adjusted the RB concentration to equal the RB concentration in RB-RH NPs ($X_{RB/PEI} = 1.0$), using the RB content: 6.8×10^{-2} mg/mg (RB mg/ RH NP mg).

To quantify the aPDT effect induced by RB-RH NPs, we examined the viability of *Streptococcus mutans* using a Microbial Viability Assay Kit-WST kit (Dojindo Laboratories, Japan). The *Streptococcus mutans* suspension (1×10^7 CFU (colony-forming units)/mL was deposited into 48-well microplates at 200 µL/well. In the experimental group, RB-RH NPs were added directly to the *Streptococcus mutans* suspension. The suspension was irradiated with white LED for 1 min. After incubation at 37 °C under anaerobic conditions for 1 h, the viability of *Streptococcus mutans* was determined using the WST assay kit according to the manufacturer's instructions.

To examine the fraction of live or dead bacteria, *Streptococcus mutans* suspension was stained using the LIVE/DEAD BacLight Bacterial Viability Kit (Thermo Fisher Scientific, Waltham, MA), following the manufacturer's instructions. Stained samples of *Streptococcus mutans* in the presence/absence of RB-RH NPs after white LED irradiation for 1 min were examined using confocal laser scanning microscopy (Biorevo BZ-9000, Keyence Co., Osaka, Japan).

Cytotoxicity assessments of RB-RH NPs under white LED irradiation

The cytotoxicity in the presence of RB-RH NPs after white LED irradiation for 1 min was evaluated on NIH3T3 cells (cultured cells isolated from fetal mouse skin) using Dojindo's Cell Counting Kit-8 (WST-8). The RB-RH NPs were added to a suspension containing 1×10^3 fibroblastic NIH3T3 cells (RIKEN BioResource Center, Tsukuba, Japan) and a culture medium (MEM alpha, GlutaMAX-I; Thermo Fisher Scientific) supplemented with 10% fetal bovine serum (Qualified FBS; Thermo Fisher Scientific) and 1% antibiotics (penicillin–streptomycin; Thermo Fisher Scientific). The suspensions were dispensed into 48-well microplates at 200 µL/well, irradiated with a white LED for 1 min, and incubated at 37 °C in a 5% CO_2 environment. After incubation for 24 h, the cytotoxicity was determined using the WST assay kit.

Results and discussion

Characterization of RH NPs

The XRD pattern of RH NPs is shown in Fig. 2a. There are no peaks derived from crystalline silica structure. The pattern is characteristic of amorphous silica with a broad diffraction peak near $2\theta = 22°$, which is consistent with typical amorphous silica [16, 36, 37]. The SEM image of RH NPs shows the size and shape were not controlled during their preparation, but the RH NPs consisted of fused NPs with small sizes of ca. 30–50 nm (Fig. 2b). The nitrogen adsorption and desorption isotherms of RH NPs had a BET surface area of 196 $m^2 \cdot g^{-1}$, a pore volume of

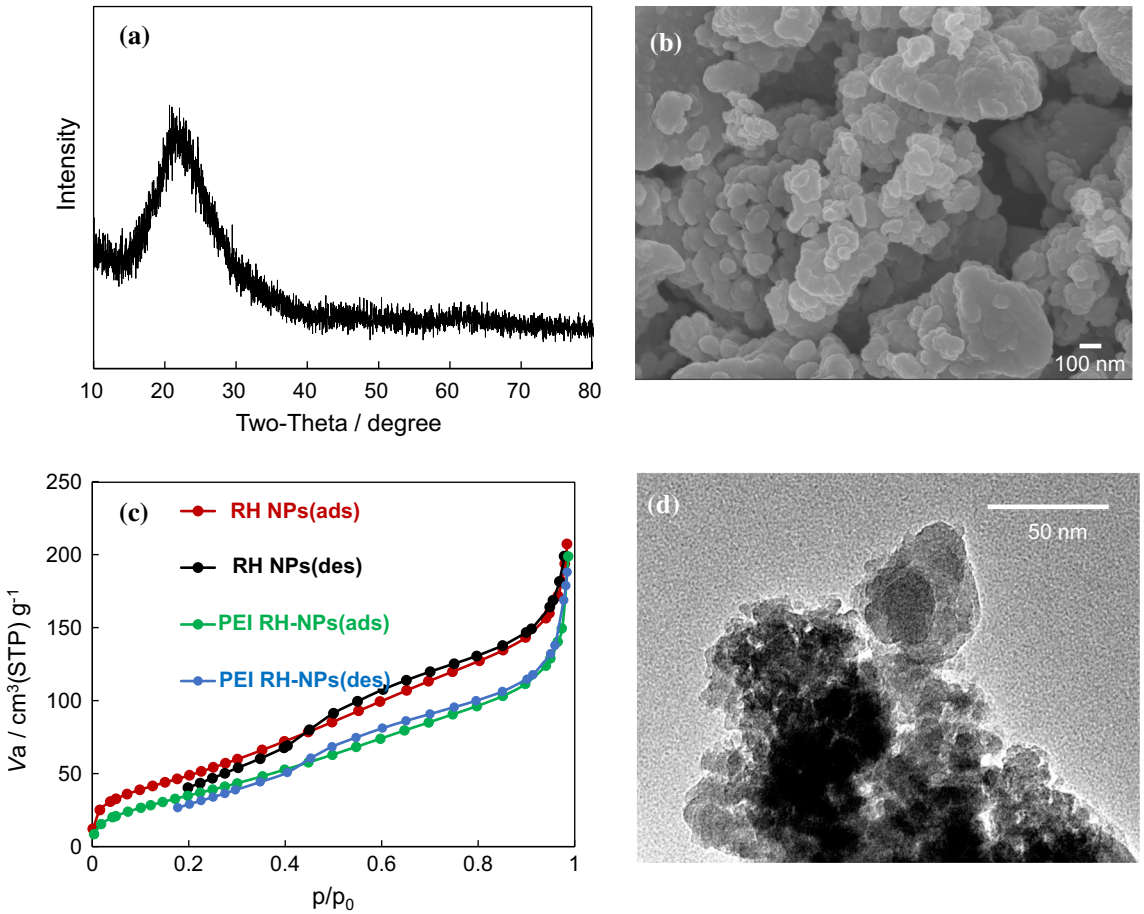

Figure 2 **a** XRD pattern of RH NPs. **b** SEM image of RH NPs. **c** Nitrogen adsorption and desorption isotherms of RH NPs (red circles: adsorption and black circles: desorption) and PEI-RH NPs (green circles: adsorption and blue circles: desorption). **d** TEM image of RH NPs.

0.32 $cm^3 \cdot g^{-1}$, and an average pore size of 6.47 nm (Fig. 2c). Herein, we suppose the RH NPs with a diameter of ca. 30 nm are non-porous solid. In that case, the specific surface area can be ca. 84 m^2/g, assuming the spherical particles without any surface contact among particles and the density of amorphous silica of 2300 kg/m^3. The larger BET surface area of RH NPs than the calculated value of non-porous solid suggests porous structures for RH NPs. The TEM image of RH NPs supports the porous nature of nano-aggregates of NPs consisting of single-nanosized NPs (< 10 nm) (Fig. 2d).

PEI-modified RH NPs

The PEI amount adsorbed on RH NPs was examined using TGA analysis. The TG curve of the PEI-modified RH-NPs showed weight loss from 0–150 °C from the water evaporation and further weight decrease from the PEI degradation above 150 °C. The amount of PEI adsorbed on RH NPs is defined as a weight loss of around 150–500 °C in the TG cures (Figure S2). The amount of PEI adsorbed on RH-NPs was 7.0×10^{-8} mol (PEI polymer unit) /mg (RH NPs) for the PEI-modified RH-NPs. We used the PEI-modified RH-NPs for further RB modification.

Figure 3a shows FT-IR spectra of PEI-modified RH-NPs, confirming the presence of PEI on the RH-NPs from the observation of the N–H (1500 cm^{-1}) and C–H bands (2800–3000 cm^{-1}) of PEI (Fig. 3a). The zeta potential value of unmodified RH NPs was − 32 mV, and the negative value originates from the dissociation of the silanol group on the silica surface. The PEI-modified RH-NPs showed a positive value of + 32 mV (Figure S3), and the charge reversal indicates the cationic PEI polymer adsorbed on negatively charged RH NPs.

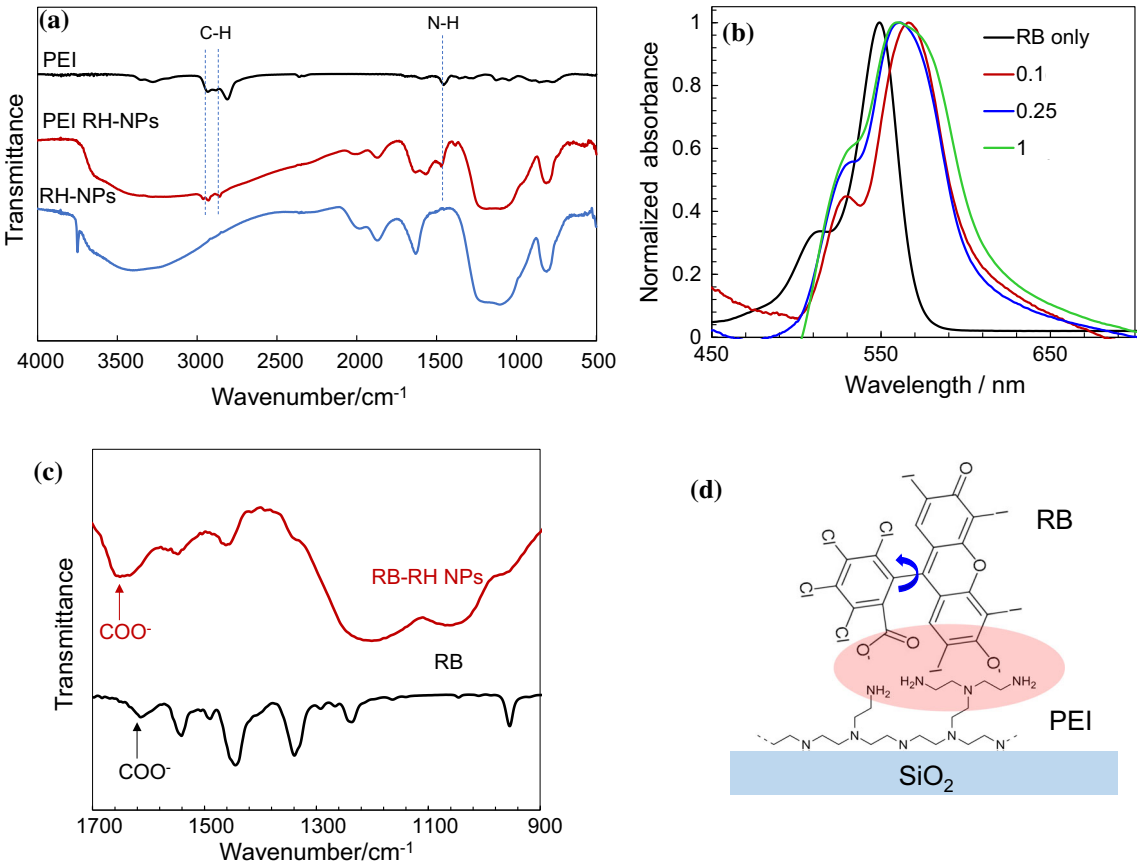

Figure 3 **a** FT-IR spectra of PEI, PEI RH-NPs, and RH-NPs. **b** Normalized absorption spectra of free RB and suspensions of RB-RH NPs with different values of XRB/PEI (XRB/PEI = 0.1, 0.25, and 1). **c** FT-IR spectra of RB and RB- RH NPs. **d** Schematic picture of possible interaction between the electrostatic interaction between the carboxylate groups of RB and PEI-modified silica surface.

The N_2 adsorption/desorption isotherms of RH NPs and PEI-modified RH NPs are shown in Fig. 2c. After the PEI adsorption on the RH NPs, the specific surface area decreases from 196 m^2g^{-1} to 146 m^2g^{-1}. The pore volume of 0.31 $cm^3 \cdot g^{-1}$ and average pore size of 8.38 nm were evaluated for PEI-modified RH-NPs, similar to unmodified RH-NPs. Thus, the PEI-modified RH-NPs maintain a high specific surface area even after the adsorption of PEI on the RH NPs.

RB-modified RH NPs (RB RH-NPs)

The control of the RB adsorption state on silica is essential for RB RH-NP photosensitizers to obtain efficient $^1O_2$ generation because the aggregation of RB quenches $^1O_2$ production. Thus, we prepared RB-RH NPs with different loading amounts of RB. We varied the molar ratio of RB with the PEI polymer unit (Mw ~ 800), $X_{RB/PEI}$ as follows: $X_{RB/PEI}$ = 0.1, 0.25, and 1.0. Figure 3b shows normalized absorption spectra of free RB and suspensions of RB-RH NPs with different values of $X_{RB/PEI}$. The free RB shows well-defined adsorption at 549 nm with a shoulder absorption at 514 nm, as expected for RB dyes. The two absorption bands of free RB in water are consistent with the reported ones: monomeric RB (549 nm) and dimeric (or aggregation) RB (515 nm) bands [38–40]. The absorption ratio of monomeric and dimeric (or aggregation) RB, A_m/A_d can be regarded as a measure of the RB aggregation. The values of (A_m/A_d) were the followings: 2.97 for RB only, 2.24 for $X_{RB/PEI}$ = 0.1, 1.79 for $X_{RB/PEI}$ = 0.25, and 1.65 for $X_{RB/PEI}$ = 1.0. The decreasing ratio with the RB loading amount suggests the aggregation of RB molecules due to the dye–dye interactions in the RB-RH NPs, which are particularly dominant in the case of RB-RH NPs ($X_{RB/PEI}$ = 0.25 and 1.0). The relatively higher value of (A_m/A_d) for RB-RH NPs ($X_{RB/PEI}$ = 0.1) suggests the suppression of the aggregates.

We also observe that the RB adsorption into the surface of PEI-modified RH NPs causes the red shift of the monomeric RB absorption from 549 nm (free RB) to 564 nm (RB-RH NPs, $X_{RB/PEI}$ = 0.1). This red-shifted absorption at 564 nm was consistent with the absorption of monomeric RB on the amine-modified silica surface, which has been reported to be the molecular deformation of RB induced by the interaction of silica surfaces [13]. The FT-IR spectra of RB-RH NPs ($X_{RB/PEI}$ = 0.1) support the physical adoption of RB on RH NPs without the chemical structural change, where the RB absorption bands are similar between RB and RB-RH NPs (Fig. 3c). However, we observed that the C=O vibration band of carboxyl groups in RB molecules shifted from 1610 cm^{-1} to 1630–1660 cm^{-1} by the RB adsorption into PEI-modified RH NPs. The result supports the electrostatic interaction between the carboxylate groups of RB and PEI-modified silica surface, as schematically shown in Fig. 3d. Thus, we can say that the optimal RB loading in monomeric form is $X_{RB/PEI}$ = 0.1 for RB-RH NPs.

Evaluation of $^1O_2$generation by RB-RH NPs

The $^1O_2$ generation efficiency can be influenced mainly by the concentration of RB molecules bound on the RH NPs. If too few RB molecules are deposited on the RH matrix, the resultant NPs may be few $^1O_2$ generations. On the other hand, if too many RB molecules are densely deposited on the RH NPs, the $^1O_2$ generation can be reduced through the $^1O_2$ self-quenching due to the RB aggregation. Thus, we have investigated the relationship between the loading amount of RB onto PEI-modified RH NPs and their $^1O_2$ generation rate of RB-RH NPs. We evaluated the $^1O_2$ generation efficiency of RB-RH NPs under white light irradiation using the $^1O_2$ detection probe ABDA. We can monitor the $^1O_2$ generation from RB-RH NPs from the absorbance decrease in ABDA by preferential reaction with $^1O_2$.

Figure 4a-4c shows the UV–Vis absorption spectra of (a) RB, (b)RB-RH NPs ($X_{RB/PEI}$ = 0.1), and (c) RB-RH NPs ($X_{RB/PEI}$ = 1.0) in the presence of ABDA under white light irradiation. The ABDA absorbance at around 300–400 nm decreased during the light irradiation, indicating $^1O_2$ generation from RB-RH NPs. We evaluated the decreasing of ABDA absorbance by reacting $^1O_2$ as the measure of $^1O_2$ generation as follows:

$$Q = \ln [A_{ABDA(t=0)}/A_{ABDA(t)}]/A_{RB}.$$

$A_{ABDA(t=0)}$ and $A_{ABDA(t)}$ are the ABDA absorbance at 379 nm before and after the light irradiation, respectively. A_{RB} is the peak absorbance of RB at 550–570 nm. Figure 4d shows the Q values of RB-RH NPs as a function of light irradiation time. A linear increase in Q values was observed in all cases. The slope of the line (=S) can be regarded as the $^1O_2$ generation rate of RB-RH NPs, as shown in Fig. 4d. The S values for RB and RB-RH NPs ($X_{RB/PEI}$ = 0.1, 0.25, and 1.0) and RB only are summarized in Fig. 5a. The S values of RB-RH NPs showed the maxima at $X_{RB/PEI}$ = 0.1, which is more prominent than that of RB. This indicates that RB-RH NPs have maximum $^1O_2$ generation efficiency at $X_{RB/PEI}$ = 0.1, corresponding to the optimal RB loading in the monomeric form on RB-RH NPs, as described above. We also examined the light intensity-dependent behavior of the $^1O_2$ generation rate for the RB-RH NPs ($X_{RB/PEI}$ = 0.1). With a higher intensity of the incident LED, a faster generation of $^1O_2$ was accomplished, confirming the photo-mediated process (Fig. 5b). Thus, it is easy to control the $^1O_2$ generation rate by changing the incident LED intensity. In contrast, the S value of RB-RH NPs ($X_{RB/PEI}$ = 0.25) is smaller than that of free RB (i.e., 0.25 times). The lower $^1O_2$ generation rate of the RB-RH NPs ($X_{RB/PEI}$ = 0.25 and 1.0) can be attributed to the RB aggregation within the RB-RH NPs. Although the enhanced mechanism of adsorbed RB on PEI-modified RH NPs at $X_{RB/PEI}$ = 0.1 is unclear at present, the coordinating bonds between the carboxylate groups of RB and the amino groups of PEI as shown in Fig. 3d could restrict the relaxation pathway of the excited RB-RH NPs by locking the RB in place, leading to fewer nonradiative decay pathways. The inhibition of nonradiative decay pathways in RB-RH NPs may enable enhanced $^1O_2$ generation.

aPDT Using RB-RH NPs under white LED irradiation

The RB-RH NPs have the $^1O_2$-generation capability under white LED irradiation. Therefore, we applied the RB-RH NPs ($X_{RB/PEI}$ = 0.1) for a-PDT against gram positive bacteria, *Streptococcus mutans*. Figure 6a shows turbidities of *Streptococcus mutans* cultures exposed to increasing doses of RB-RH NPs ($X_{RB/PEI}$ = 0.1) with LED irradiation at a range of concentrations (0 (absence), 1, 5, and 10 mg/mL). The

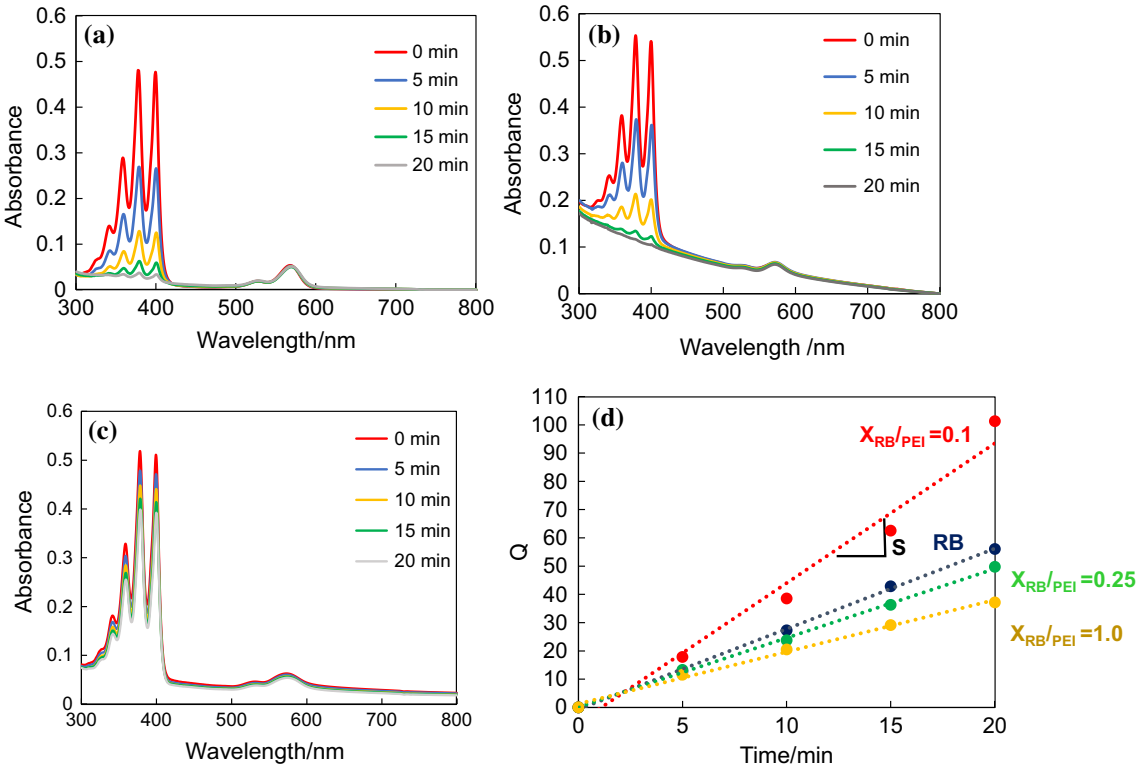

Figure 4 UV–Vis spectra of ABDA during white LED irradiation in the presence of **a** RB, **b** RB-RH NPs (XRB/PEI = 0.1, and **c** RB-RH NPs (XRB/PEI = 1.0). **d** Normalized ABDA absorbance at 379 nm (*Q*) as a function of irradiation time in the presence of RB or RB-RH NPs (XRB/PEI = 0.1, 0.25, and 1.0).

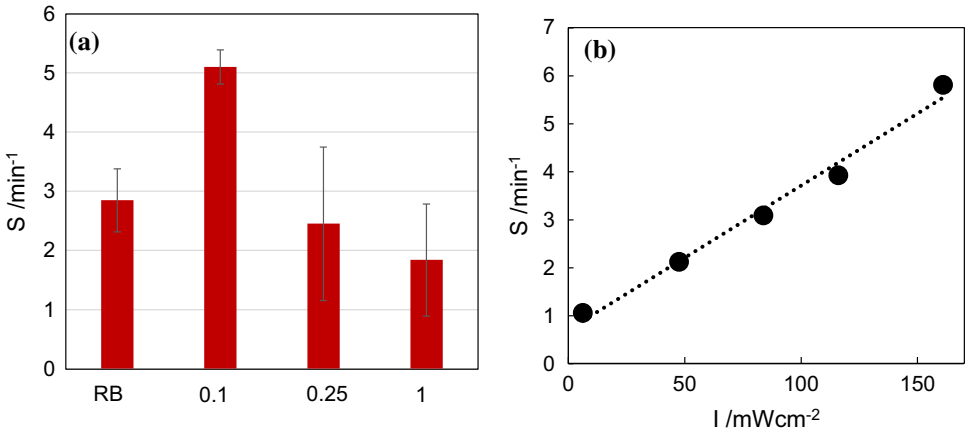

Figure 5 **a** $^1O_2$ generation efficiency (*S*) of RB and RB-RH NPs (XRB/PEI = 0.1, 0.25, and 1.0). **b** The values of *S* as a function of the white light irradiation intensity.

turbidity directly reflects the growth over time of the bacterial population in the suspension. Low turbidity indicates a small number of bacteria in the suspension. With LED irradiation, exposure to RB-RH NPs resulted in the decrease in turbidities. Thus, photoexcited 1 mg/mL RB-RH NPs significantly reduced the turbidity of *Streptococcus mutans* cultures (Fig. 6a). These results suggested that RB-RH NPs at concentrations of 1 mg/mL were effective for aPDT in this experimental system.

To examine the conjugating effect of RB and RH NPs, we compared aPDT activity of RB-RH NPs and RB alone. The RB-RH NPs ($X_{RB/PEI}$ = 1.0) were estimated to include 6.8×10^{-2} mg RB /RH NP mg from the RB adsorption experiment. Even without LED irradiation, the decrease in turbidity was observed after 24 h in the presence of the RB-RH NPs (the

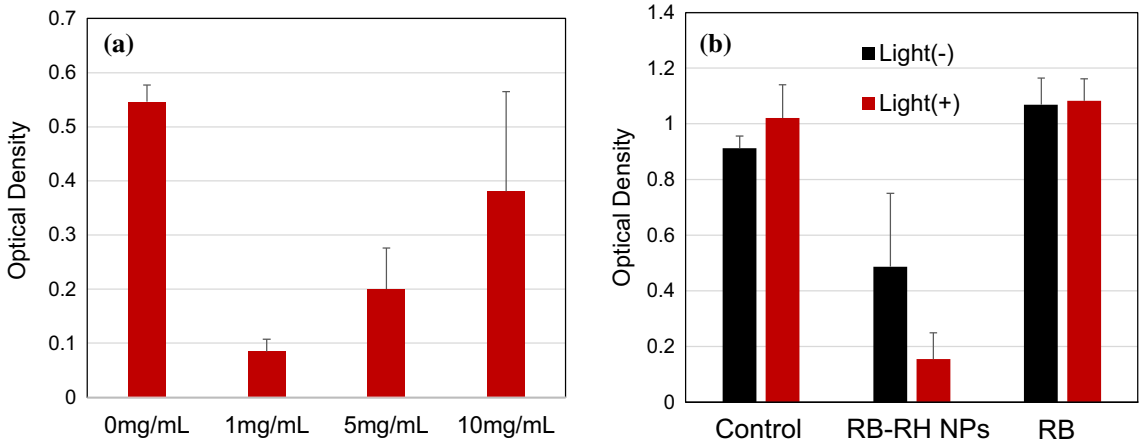

Figure 6 **a** Dose-Dependent antimicrobial effects of RB-RH NPs (XRB/PEI = 0.1) on *Streptococcus mutans* (ATCC 35,668) under white LED irradiation for 1 min after 24 h incubation (n = 5, mean ± standard deviation). *$P < 0.05$ vs other groups. **b** Antimicrobial effects of RB (6.8×10^{-2} mg/mL) and RB-RH NPs (XRB/PEI = 1.0) (1 mg/mL) on *Streptococcus mutans* (ATCC 35,668) under white LED irradiation for 1 min after 24 h incubation (n = 5, mean ± standard deviation). *$P < 0.05$ vs other groups.

concentration of RB, 6.8 μg/mL), indicating the antimicrobial effect of RB-RH NPs themselves without the LED light. However, under white LED irradiation in the presence of the RB-RH NPs, a further decrease in the turbidity of the bacterial suspensions occurred, indicating the suppression of bacterial growth (i.e., a-PDT activity). The $^1O_2$ generated by photoexcited RB-RH NPs likely suppressed *Streptococcus mutans* growth. For comparison, we also examined antibacterial tests on RB only. We adjusted the RB concentration to equal the RB concentration in RB-RH NPs ($X_{RB}/_{PEI}$ = 1.0), using the RB adsorption mass per mg of RH NPs: 6.8×10^{-2} mg/mg. The aPDT activity of RB-RH NPs was higher than that of free RB by the combined effect of RB with RH NPs (Fig. 6b). The result demonstrates that RB-RH NPs are promising photosensitizers for aPDT applications. Thus, our RB-RH NPs appear to possess greater antibacterial potency against *Streptococcus mutans* than that obtained with RB alone.

To further quantify these effects of aPDT induced by RB-RH-NP irradiation, we also examined the viability of *Streptococcus mutans* by using a Microbial Viability Assay Kit-WST kit. According to the microbial viability data in Fig. 7a, the light-induced killing bacteria is observed in the presence of RB-RH NPs. The LIVE/DEAD staining observations showed that samples after white LED irradiation consistently exhibited green fluorescence (live bacteria) (Fig. 7c). In contrast, dead bacteria after white LED irradiation, as shown by the yellow/orange fluorescence, are predominantly observed in the presence of the RB-RH NPs (Fig. 7d). The LIVE/DEAD test thus supports the aPDT activity of RB-RH-NPs on *Streptococcus mutans*.

It is well known that cytotoxic biomaterials reduce WST-8[41]. We evaluated the cytotoxicity of NIH3T3 cells (cultured cells isolated from fetal mouse skin) after white LED irradiation for 1 min in the presence of RB-RH NPs using WST-8 (Fig. 7b). There is a meaningful difference in the viability of NIH3T3 cells between the control (no RB-RH NPs) and RB-RH NPs, but the viability decrease in NIH3T3 cells is smaller than that of *Streptococcus mutans*. This suggests that aPDT action of RB-RH NPs is more efficient for *Streptococcus mutans* than NIH3T3 cells.

Conclusion

We fabricated a novel photosensitizer based on rose Bengal (RB)-decorated rice husk-derived silica nanoparticles (RH NPs) to enhance $^1O_2$ generation for antimicrobial photodynamic inactivation. The polyethyleneimine (PEI)-modified RH NPs to conjugate RB through the electrostatic interaction were prepared to yield RB-modified RH NPs (RB-RH NPs). We have investigated the relationship between the loading amount of RB onto PEI-modified RH NPs and their $^1O_2$ generation rate of RB-RH NPs (i.e., $^1O_2$ generation efficiency). The RB-RH NPs have

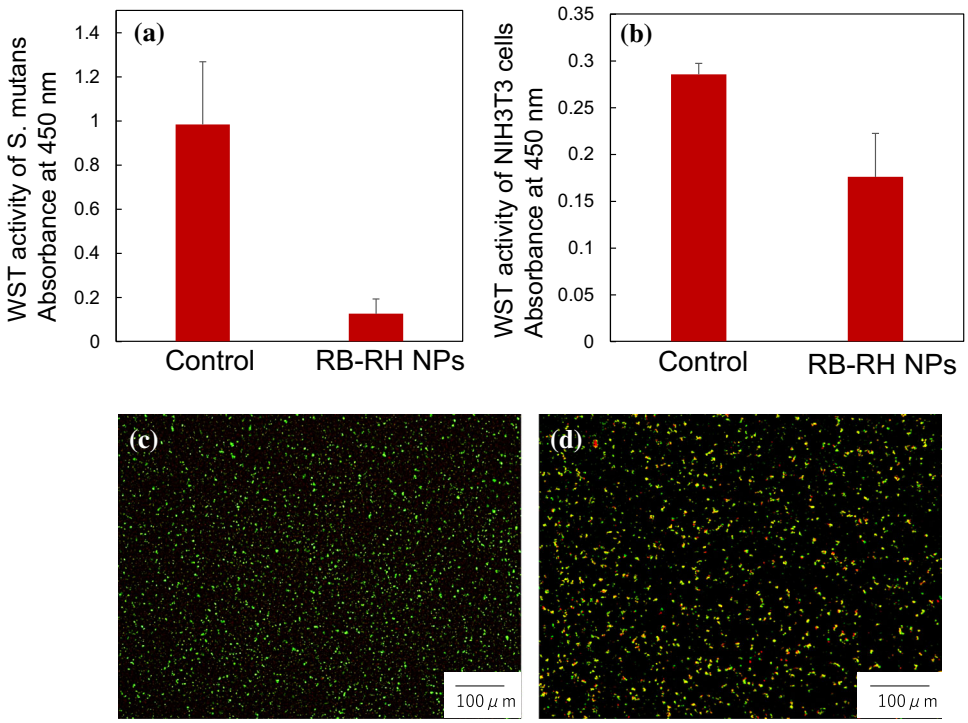

Figure 7 **a** WST-8 activity for *Streptococcus mutans* after white LED irradiation for 1 min in the absence (control) and in the presence of RB-RH NPs(XRB/PEI = 0.1, 1 mg/mL) (n = 4). **b** Cytotoxicity assessments of NIH3T3 cells using WST-8 after white LED irradiation for 1 min in the absence (control) and in the presence of RB-RH NPs (XRB/PEI = 0.1, 1 mg/mL) (n = 6). Fluorescence examination of the labeled *Streptococcus mutans* with the LIVE/ DEAD kit after white LED irradiation for 1 min **c** in the absence (control) and **d** in the presence of RB-RH NPs (XRB/PEI = 0.1, 1 mg/mL).

maximum $^1O_2$ generation efficiency at the molar ratio of RB/PEI polymer, $X_{RB/PEI}$ = 0.1, corresponding to the optimal RB loading in the monomeric form on RB-RH NPs. In contrast, high loading RB with more than of $X_{RB/PEI}$ = 0.25, the overall $^1O_2$ generation efficiency is reduced through the $^1O_2$ self-quenching due to the RB aggregation. The RB-RH NPs have significant antimicrobial activity on *Streptococcus mutans* when compared to free RB after white light irradiation. The RB-RH NP-based aPDT can be employed effectively in the treatment of *Streptococcus mutans*.

Acknowledgements

This work was financially supported by the JSPS KAKENHI under Grant No. JP 20K21095 and 22H01915. This research was also financially supported by the Kansai University Fund for Collaborative Research of Engineering, Medicine, and Pharmacology, 2022 and the Joint Usage/Research Center on Joining and Welding, Osaka University.

Declarations

Conflict of interest The authors declare that they have no known competing financial interests or personal relationships that could have appeared to influence the work reported in this paper.

Ethical statement This work involves no live subjects (human or animal).

Supplementary Information: The online version contains supplementary material available at https://doi.org/10.1007/s10853-023-08194-z.

References

[1] Schwarz S, Kehrenberg C, Walsh TR (2001) Use of antimicrobial agents in veterinary medicine and food animal production. Int J Antimicrob Agents 17:431–437. https://doi.org/10.1016/S0924-8579(01)00297-7

[2] Ogunsona EO, Muthuraj R, Ojogbo E, Valerioc O, Mekonnen TH (2020) Engineered nanomaterials for antimicrobial applications: a review. Appl Mater Today 18:100473. https://doi.org/10.1016/j.apmt.2019.100473

[3] Rawson TM, Ming D, Ahmad R, Moore LP, Holmes AH (2020) Antimicrobial use, drug-resistant infections and COVID-19. Nat Rev Microbiol 18:409–410. https://doi.org/10.1038/s41579-020-0395-y

[4] Annunziato G (2019) Strategies to overcome antimicrobial resistance (AMR) making use of non-essential target

inhibitors: a review. Int J Mol Sci 20:5844. https://doi.org/10.3390/ijms20235844

[5] Hu X, Zhang H, Wang Y et al (2022) Synergistic antibacterial strategy based on photodynamic therapy: progress and perspectives. Chem Eng J 450:138129. https://doi.org/10.1016/j.cej.2022.138129

[6] Nguyen VN, Zhao Z, Tang BZ, Yoon J (2022) Organic photosensitizers for antimicrobial phototherapy. Chem Soc Rev 51:3324–3340. https://doi.org/10.1039/d1cs00647a

[7] Sabino CP, Wainwright M, Ribeiro MS, Sellera FP, Anjos C, Baptista MS, Lincopan N (2020) Global priority multidrug-resistant pathogens do not resist photodynamic therapy. J Photochem Photobiol B Biol 208:111893. https://doi.org/10.1016/j.jphotobiol.2020.111893

[8] Qi M, Chi M, Sun X et al (2019) Novel nanomaterial-based antibacterial photodynamic therapies to combat oral bacterial biofilms and infectious diseases. Int J Nanomedicine 14:6937–6956. https://doi.org/10.2147/IJN.S212807

[9] Yu XT, Sui SY, He YX, Yu CH, Peng Q (2022) Nanomaterials-based photosensitizers and delivery systems for photodynamic cancer therapy. Biomater Adv 135:212725. https://doi.org/10.1016/j.bioadv.2022.212725

[10] Thomas-Moore BA, del Valle CA, Field RA, Marín MJ (2022) Recent advances in nanoparticle-based targeting tactics for antibacterial photodynamic therapy. Photochem Photobiol Sci 21:1111–1131. https://doi.org/10.1007/s43630-022-00194-3

[11] Kawawaki T, Negishi Y, Kawasaki H (2020) Photo/electrocatalysis and photosensitization using metal nanoclusters for green energy and medical applications. Nanoscale Adv 2:17–36. https://doi.org/10.1039/c9na00583h

[12] Couleaud P, Morosini V, Frochot C, Richeter S, Raehm L, Durand JO (2010) Silica-based nanoparticles for photodynamic therapy applications. Nanoscale 2:1083–1095. https://doi.org/10.1039/c0nr00096e

[13] Martins Estevão B, Cucinotta F, Hioka N et al (2015) Rose Bengal incorporated in mesostructured silica nanoparticles: structural characterization, theoretical modeling and singlet oxygen delivery. Phys Chem Chem Phys 17:26804–26812. https://doi.org/10.1039/c5cp03564c

[14] Nakamura T, Son A, Umehara Y, Ito T, Kurihara R, Ikemura Y, Tanabe K (2016) Confined singlet oxygen in mesoporous silica nanoparticles: selective photochemical oxidation of small molecules in living cells. Bioconjug Chem 27:1058–1066. https://doi.org/10.1021/acs.bioconjchem.6b00061

[15] Mendoza C, Désert A, Khrouz L, Páez CA, Parola S, Heinrichs B (2021) Heterogeneous singlet oxygen generation: in-operando visible light EPR spectroscopy. Environ Sci Pollut Res 28:25124–25129. https://doi.org/10.1007/s11356-019-04763-5

[16] Saita S, Anzai M, Mori N, Kawasaki H (2021) Controlled aggregation of methylene blue in silica–methylene blue nanocomposite for enhanced $^1O_2$ generation. Colloids Surf A Physicochem Eng Asp 617:126360. https://doi.org/10.1016/j.colsurfa.2021.126360

[17] Tamtaji M, Kazemeini M (2022) Enhanced singlet oxygen production under nanoconfinement using silica nanocomposites towards improving the photooxygenation's conversion. J Nanoparticle Res 24:1–17. https://doi.org/10.1007/s11051-022-05553-w

[18] Uppal A, Jain B, Gupta PK, Das K (2011) Photodynamic action of rose bengal silica nanoparticle complex on breast and oral cancer cell lines. Photochem Photobiol 87:1146–1151. https://doi.org/10.1111/j.1751-1097.2011.00967.x

[19] Gupta PK, Das K, Sharma M (2014) Effect of complexing with silica nanoparticles on the phototoxicty of some photosensitisers. Procedia Eng 92:9–18. https://doi.org/10.1016/j.proeng.2013.09.249

[20] Kabanov V, Press DJ, Huynh RPS, Shimizu GKH, Heyne B (2018) Assessment of encapsulated dye's distribution in silica nanoparticles and their ability to release useful singlet oxygen. Chem Commun 54:6320–6323. https://doi.org/10.1039/c8cc03413c

[21] Kohle FFE, Li S, Turker MZ, Wiesner UB (2020) Ultrasmall PEGylated and Targeted core-shell silica nanoparticles carrying methylene blue photosensitizer. ACS Biomater Sci Eng 6:256–264. https://doi.org/10.1021/acsbiomaterials.9b01359

[22] Kabanov V, Heyne B (2020) Impact of incoherent coupling within localized surface plasmon resonance on singlet oxygen production in rose bengal-modified silica-coated silver nanoshells (SiO_2@Ag@SiO_2-RB). ACS Appl Nano Mater 3:8126–8137. https://doi.org/10.1021/acsanm.0c01544

[23] Toum Terrones Y, Torresán MF, Mirenda M, Rodríguez HB, Wolosiuk A (2022) Photoactive red fluorescent SiO_2 nanoparticles based on controlled methylene blue aggregation in reverse microemulsions. Langmuir 38:6786–6797. https://doi.org/10.1021/acs.langmuir.1c02458

[24] Alam MM, Hossain MA, Hossain MD et al (2020) The potentiality of rice husk-derived activated carbon: from synthesis to application. Processes 8:203. https://doi.org/10.3390/pr8020203

[25] Kim S, Park JY, Gu YM et al (2021) Eco-friendly and facile synthesis of size-controlled spherical silica particles from rice husk. Nanoscale Adv 3:6965–6973. https://doi.org/10.1039/d1na00668a

[26] Wang Z, Smith AT, Wang W, Sun L (2018) Versatile nanostructures from rice husk biomass for energy applications. Angew Chem Int Ed 57:13722–13734. https://doi.org/10.1002/anie.201802050

[27] Shen Y (2017) Rice husk silica derived nanomaterials for sustainable applications. Renew Sustain Energy Rev 80:453–466. https://doi.org/10.1016/j.rser.2017.05.115

[28] Sharma P, Prakash J, Kaushal R (2022) An insight into the green synthesis of SiO2 nanostructures as a novel adsorbent for removal of toxic water pollutants. Environ Res 212:113328. https://doi.org/10.1016/j.envres.2022.113328

[29] Rajanna SK, Kumar D, Vinjamur M, Mukhopadhyay M (2015) Silica aerogel microparticles from rice husk ash for drug delivery. Ind Eng Chem Res 54:949–956. https://doi.org/10.1021/ie503867p

[30] Alshatwi AA, Athinarayanan J, Periasamy VS (2015) Biocompatibility assessment of rice husk-derived biogenic silica nanoparticles for biomedical applications. Mater Sci Eng C 47:8–16. https://doi.org/10.1016/j.msec.2014.11.005

[31] Park JY, Mun W, Chun J, Sang BI, Mitchell RJ, Lee JH (2022) Alkali extraction to detoxify rice husk-derived silica and increase its biocompatibility. ACS Sustain Chem Eng 10:7811–7817. https://doi.org/10.1021/acssuschemeng.2c01307

[32] Demartis S, Obinu A, Gavini E, Giunchedi P, Rassu G (2021) Nanotechnology-based rose bengal: a broad-spectrum biomedical tool. Dye Pigment 188:109236. https://doi.org/10.1016/j.dyepig.2021.109236

[33] Gianotti E, Martins Estevão B, Cucinotta F, Hioka N, Rizzi M, Ren F, Marchese L (2014) An efficient rose bengal based nanoplatform for photodynamic therapy. Chem A Eur J 20:10921–10925. https://doi.org/10.1002/chem.201404296

[34] Alqerban A (2021) Effectiveness of riboflavin and rose bengal photosensitizer modified adhesive resin for orthodontic bonding. Pharmaceuticals 14:48. https://doi.org/10.3390/ph14010048

[35] Hirose M, Yoshida Y, Horii K, Hasegawa Y, Shibuya Y (2021) Efficacy of antimicrobial photodynamic therapy with rose bengal and blue light against cariogenic bacteria. Arch Oral Biol 122:105024. https://doi.org/10.1016/j.archoralbio.2020.105024

[36] Umeda J, Kondoh K (2008) High-purity amorphous silica originated in rice husks via carboxylic acid leaching process. J Mater Sci 43:7084–7090. https://doi.org/10.1007/s10853-008-3060-9

[37] Umeda J, Kondoh K (2010) High-purification of amorphous silica originated from rice husks by combination of polysaccharide hydrolysis and metallic impurities removal. Ind Crops Prod 32:539–544. https://doi.org/10.1016/j.indcrop.2010.07.002

[38] Oscar VA, Neckers DC (1989) Aggregation phenomena in xanthene dyes. Acc Chem Res 22:171–177. https://doi.org/10.1021/ar00161a002

[39] Serrano MP, Rafti M, Thomas AH, Borsarelli CD (2019) Photosensitizing properties of hollow microcapsules built by multilayer self-assembly of Poly(allylamine hydrochloride) modified with rose bengal. RSC Adv 9:19226–19235. https://doi.org/10.1039/c9ra03153g

[40] Mendes B, Kassumeh S, Aguirre-Soto A, Pei Q, Heyne B, Kochevar IE (2021) Influence of rose bengal dimerization on photosensitization. Photochem Photobiol 97:718–726. https://doi.org/10.1111/php.13379

[41] Okamoto I, Miyaji H, Miyata S, Shitomi K, Sugaya T, Ushijima N, Akasaka T, Enya S, Saita S, Kawasaki H (2021) Antibacterial and antibiofilm photodynamic activities of lysozyme-Au nanoclusters/rose bengal conjugates. ACS Omega 6:9279–9290. https://doi.org/10.1021/acsomega.1c00838